Effects of the 2007 Martian Global Dust Storm on Boundary Positions in the Induced Magnetosphere

Catherine E. Regan, Andrew J. Coates, Mark Lester, Anne Wellbrock, Geraint H. Jones, Beatriz Sánchez-Cano, Philippe Garnier, Richard P. Haythornthwaite, Dikshita Meggi, Rudy A. Frahm, et al.

The Planetary Science Journal, 5:130 (16pp), 2024 June https://doi.org/10.3847/PSJ/ad4116

Effects of the 2007 Martian Global Dust Storm on Boundary Positions in the Induced Magnetosphere

Catherine E. Regan[1,2], Andrew J. Coates[1,2], Mark Lester[3], Anne Wellbrock[1,2], Geraint H. Jones[1,2], Beatriz Sánchez-Cano[3], Philippe Garnier[4], Richard P. Haythornthwaite[1,2], Dikshita Meggi[3], Rudy A. Frahm[5], and Mats Holmström[6]
[1] Mullard Space Science Laboratory, Department of Space and Climate Physics, University College London, UK; catherine.regan.19@ucl.ac.uk
[2] Centre for Planetary Sciences at UCL and Birkbeck, London, UK
[3] School of Physics and Astronomy, University of Leicester, UK
[4] IRAP, Toulouse, France
[5] Southwest Research Institute, TX, USA
[6] Swedish Institute of Space Physics, Kiruna, Sweden
Received 2023 June 6; revised 2024 April 17; accepted 2024 April 18; published 2024 June 5

Abstract

Mars's magnetosphere is a sensitive system, varying due to external and internal factors, such as solar wind conditions and crustal magnetic fields. A signature of this influence can be seen in the position of two boundaries; the bow shock and the induced magnetospheric boundary (IMB). The bow shock moves closer to Mars during times of high solar activity, and both the bow shock and IMB bulge away from Mars over crustal magnetic fields in the southern hemisphere. This study investigates whether large-scale atmospheric events at Mars have any signature in these two magnetic boundaries, by investigating the 2007 storm. The 2007 global storm lasted for several months and increased atmospheric temperatures and densities of both water vapor and carbon dioxide in the atmosphere, leading to an increase in atmospheric escape. Using Mars Express, we identified boundary locations before, during, and after the event, and compared these to modeled boundary locations and areographical locations on Mars. We find that, while it is unclear whether the bow shock position is impacted by the storm, the IMB location does change significantly, despite the orbital bias introduced by Mars Express. The terminator distance for the IMB peaks at longitudes 0°–40° and 310°–360°, leaving a depression around 180° longitude, where the boundary usually extends to higher altitudes due to the crustal magnetic fields. We suggest this may be due to the confinement of ionospheric plasma over crustal fields preventing mixing with the dust, creating a dip in ionospheric pressure here.

Unified Astronomy Thesaurus concepts: Mars (1007); Planetary magnetospheres (997); Planetary science (1255); Planetary ionospheres (2185); Surface processes (2116)

1. Introduction

As Mars lacks a global magnetic field, the induced magnetosphere of Mars is a sensitive environment that is influenced by external and internal variability. External influences include solar wind and solar irradiance conditions that can cause boundaries in the magnetosphere to fluctuate in their position relative to the surface. When the solar wind increases in density and speed, boundaries move closer to the surface as solar wind pressure increases on the topside of the magnetosheath (Brain et al. 2005). This is also the case with solar events such as coronal mass ejections (Vignes et al. 2000; Halekas et al. 2017; Neves-Amaral et al. 2019). The bow shock has a strong variability with solar cycle (Hall et al. 2016, 2019), being closer to the surface of Mars at solar maximum and farther from the surface at solar minimum. The structure of the bow shock changes as the angle between the interplanetary magnetic field (IMF) and local shock normal changes (Garnier et al. 2022a). These external influences can affect boundary positions over short and long timescales (hours for solar events and years for variations in the solar cycle). The variation in the space environment over a Martian year is highly influential, and can change bow shock boundary positions by as much as 11% (Hall et al. 2016). Looking internally at Mars, there are also phenomena that can influence the environment. Although Mars has no global magnetic field, areas of the crust have rocks holding onto remanent magnetization from four billion years ago, when it is believed that a global dynamo was present (Acuna et al. 1998; Connerney et al. 2001). These crustal magnetic fields form "mini-magnetospheres" and can increase the altitudes of boundaries over these areas (Mitchell et al. 2001; Fang et al. 2017; Garnier et al. 2022b).

Another potential source of variability for the boundaries is the weather on Mars, which is highly influenced by the transportation of water vapor (Fedorova et al. 2021) and other atmospheric gases such as carbon dioxide, which are being lost to space as the population becomes ionized by the solar wind (Frahm et al. 2010; Chaufray et al. 2021). The density of these gases increases substantially during the dust season on Mars, which occurs in the southern hemispheric summer. The orbit of Mars around the Sun is extremely eccentric (value of 0.09) (Barlow 2008), with the flux of solar radiation peaking at perihelion. This coincides with the southern hemisphere solstice, resulting in a strong asymmetry in seasonal effects, which causes the Martian dust season. During this time of year, dust storms are very common. Occasionally, these storms can grow into one planet-wide storm system, lasting several months. These dust storms cause water vapor and carbon

dioxide to be lifted to high altitudes, causing a spike in atmosphere loss from the planet (Chaffin et al. 2021; Kimura et al. 2022). This study investigates whether these processes can be seen higher up in the induced magnetosphere.

1.1. Mars's Induced Magnetosphere

Mars's induced magnetosphere forms when the solar wind interacts with the Martian exosphere and ionosphere (Nagy et al. 2004). This external, supersonic flow of plasma is deflected around the planet, and this deflection begins at the bow shock boundary. This is the outer boundary of the Martian plasma system. Here, solar wind thermalizes and slows to subsonic speeds. It is characterized by an enhancement of magnetic field draping and mass loading of plasma as the solar wind increases in temperature and increases in total density. The bow shock is located at altitudes of approximately 0.58 R_M to 1.6 R_M on average, at the subsolar and terminator point, respectively (Bertucci et al. 2011), where $R_M = 3390$ km is the radius of Mars. Studies by Hall et al. (2019) found that the location of the bow shock varies by 7% over the 11 yr solar cycle, and by 11% over a Martian year, showing that it is a highly variable boundary.

The magnetosheath is the region between the bow shock and the induced magnetospheric boundary (IMB). It is populated by solar wind plasma that is decelerated, heated, and compressed at the bow shock, and is filled with ultra-low-frequency plasma waves that are observed up to the IMB (Bertucci et al. 2011). The IMB separates the slowed solar wind plasma from the planetary plasma population. The IMB, sometimes referred to as the magnetic pile-up boundary, is a sharp, distinct discontinuity, with the magnetic field showing increasing magnitude, decreasing fluctuations, and increased draping. In addition to electrons decreasing in temperature, the total density increases and the solar wind ion density decreases when moving from the magnetosheath into the planetary plasma region (Bertucci et al. 2011). The IMB altitude is located on average at 0.33 R_M to 0.45 R_M at the subsolar and terminator points, respectively. Immediately upstream of the IMB, significant mass loading may occur as newly ionized particles become accelerated and approach the boundary. Brain et al. (2005) first found that this boundary is located further from Mars during perihelion.

The next boundary close to the surface of Mars is the ionopause, which marks the upper boundary of the ionosphere. The ionosphere is formed when solar radiation ionizes atmospheric particles by photoionization. The atmosphere, which is mostly carbon dioxide, transitions to oxygen and hydrogen where the solar wind interacts with the planet. The ionosphere is also lost into space through many mechanisms, such as solar-wind-related pickup-ion processes (Shinagawa & Cravens 1989) and ionization escape (Frahm et al. 2006a, 2006b, 2010). The total pressure of the ionosphere (thermal + magnetic) is balanced with the dynamic pressure of the solar wind (Sánchez-Cano et al. 2020), and the ionospheric peak can be located at an altitude of 130–170 km above the Martian surface (Zhang et al. 1991; Withers 2009). This boundary is influenced by the crustal magnetic fields, the altitude of the ionopause depends on external factors such as the dynamic pressure of the solar wind (Sánchez-Cano et al. 2020), and a sharp ionopause boundary may not always be present. The same authors found that the ionopause is frequently observed over areas of nonmagnetic crust. The occurrence of the ionopause can also vary with season, including dust storm seasons (Duru et al. 2020). Xu et al. (2023) suggest that the photoelectron boundary at Mars marks the top of the ionosphere on the dayside, and the boundary where plasma from the magnetosheath deflects around Mars going downstream, which serves as a new means of measuring the ionopause and photoelectron boundary.

Closer to the planet, the Martian atmosphere and exosphere produce ions via photoionization and impact ionization between the solar wind and the atmospheric gases (Nagy et al. 2004). This deposits energy into the upper atmosphere of Mars, increasing ionization and UV emissions. The exosphere is responsive to changes in heat flux in the thermosphere, with increasing heat flux causing an increase in exospheric ion pickup in this region. Bertucci et al. (2013) showed that the exosphere's seasonal expansion during perihelion increased the occurrence rate of waves generated from exospheric proton pickup, which was confirmed by Romanelli et al. (2015). The increased solar EUV flux during perihelion in the thermosphere causes the expansion of the exosphere (Bhattacharyya et al. 2015; Halekas et al. 2017).

1.2. Dust Storms

Mars experiences a dust storm season every Mars year (687 Earth days) during the southern hemisphere's summer, when Mars is around perihelion. During this season, regional dust storms are very common and large amounts of dust are lofted high into the atmosphere by strong winds. Occasionally, these regional storms can grow and merge to form a planet-wide event, where the entire globe is covered in one storm system. The last three such events occurred in 2018, 2007, and 2001. The interannual variability of the Martian climate as a whole is largely dominated by the interannual variability of global storms during the southern hemispheric summer (Shirley 2015).

Global-scale dust storms on Mars can cause atmospheric warming of 30–40 K, and the heating from dust particles causes CO_2 to dominate throughout a larger altitude range in the atmosphere than normal (Fedorova et al. 2018). This enhances the photoelectron flux that is seen at altitudes of approximately 400 km (Xu et al. 2015). In crustal magnetic field regions, the net upward motion of plasma causes an enhancement of electron density and an increase in the altitude of the peak electron density. During storm development, the ionization and electric fields in the lower atmosphere decreases as the amount of UV radiation reaching the surface decreases (Venkateswara Rao et al. 2019). This consequently increases the mixing of dust aerosols. Dust storms can also increase the ionospheric peak altitude by 10–20 km (Felici et al. 2020). Ionization moved higher in altitude during the global dust storm of 2007, seen in radar echoes using the Mars Advanced Radar for Subsurface and Ionsopheric Sounding (MARSIS) instrument on board Mars Express (Venkateswara Rao et al. 2019).

Dust can influence the temperature of the atmosphere up to 80 km in altitude (Kleinböhl et al. 2014), and therefore can also influence the behavior of individual species and particles, which increases atmospheric escape as shown by the increase in hydrogen loss during the MY28 (2007) global dust storm (Chaffin et al. 2021). During the same storm, at solar longitude (L_S) 270°, the densities of water vapor and carbon dioxide had increased several times, with values of water vapor concentration ranging from a 2–5 times increase in the southern hemisphere to a 10 times increase in the northern hemisphere

at solar longitudes 268°–285°, (Fedorova et al. 2018). The water from the warm southern hemisphere was transferred to the north of the planet through atmospheric circulation. The increase in water vapor density was short-lived, lasting around 1 month during the global storm.

The 2007 storm became global in mid-July, and normal surface conditions had recovered by mid-October, but there were several different stages of growth and decline over the three months. Observations of the 2007 storm from the Mars Climate Sounder instrument (McCleese et al. 2007) on board the Mars Reconnaissance Orbiter (Zurek & Smrekar 2007) looked at the dust and temperature profiles, and at L_S 256° (June 12), dust began to be lofted to altitudes of 35–40 km (Kleinböhl et al. 2014). Regional dust began lifting at L_S 261.°8 (June 21) in the southern mid-latitudes near the Noachis/West Hallas region of Mars, in addition to the development of a single storm from the Chryse region (Wang & Richardson 2015; Fedorova et al. 2018). The storm then went into an expansion phase, with the dust lifting higher into the Martian atmosphere and an increase in wind speeds. Thirteen sols (Martian days) later (L_S 269.°3 July 3), global lifting began. The following days saw dust loading increase throughout the atmosphere, and in the southern hemisphere temperatures rose from near normal (180 K) to over 220 K at the surface. By L_S 275° (July 12), the dust storm became global and temperatures rose to up to 240 K at high latitudes and over the north pole. High temperatures were recorded here, in addition to a lower dust opacity when compared to the rest of the planet. This result was suggested by Kleinböhl et al. (2014) to be due to the adiabatic heating in the meridional circulation of Mars as opposed to solar heating of dust. This circulation on Mars is strongly enhanced during global-scale storms, causing the increase in temperature observed at the north pole during the 2007 storm. The expansion phase ended at L_S 275.°2 (July 12), at which point the planet was encircled in a haze covering the entire southern hemisphere and the majority of the northern hemisphere (Fedorova et al. 2018). By L_S 280° (July 20), dust began falling. At L_S 285° (285), the levels of dust at 35–40 km in altitude had decreased as the decay phase began. The storm ended at L_S 320°–330° (September 25–October 13), with the temperature and dust levels on the surface returning to normal, non-dusty conditions (Kleinböhl et al. 2014).

In this paper, we investigate whether the effect of the 2007 global dust storm can be seen in the magnetosphere. Previous studies (Kleinböhl et al. 2014; Fedorova et al. 2018; Venkateswara Rao et al. 2019; Chaffin et al. 2021) show that global dust storms impact the atmosphere and ionosphere, and this study looks at whether it has an effect on the IMB and bow shock. The following sections introduce our data set from Mars Express and how we study the two boundaries (Section 2), our methodology to model these boundaries using Mars Express crossings (Section 3), and a comparison with data from the MARSIS instrument (Section 5). We then bring these methods together for analysis (Section 6).

2. Instrumentation and Data Sampling

2.1. Mars Express

The Mars Express satellite was launched in 2003 after a rapid planning and building stage led by the European Space Agency. After over six months of travel, the orbiter entered Mars's orbit on 2003 December 25 and began science operations in early 2004. It is still operational (at the time of writing) and has been sending back scientific data for nearly 20 Earth years, with the nominal mission lasting 1 Martian year. Mars Express orbits Mars with a period of 7 hr, with a pericenter and apocenter of 330 km and 10,530 km, respectively, at an orbital inclination of 86.°9.

We use electron and ion data from the Analyser of Space Plasmas and EneRgetic Atoms (ASPERA-3) experiment on board Mars Express (Barabash et al. 2006). ASPERA-3 contains four instruments to measure and detect different particles at varying flux energies to obtain characteristics and distributions of particles in this environment. ASPERA-3 has two energetic neutral atom instruments and an electron spectrometer (ELS) that can measure electrons with energies up to 20 keV q^{-1}, with a full azimuthal angular coverage from 16 individual nodes, covering 22.°5 each, with an energy resolution ($\Delta/E = 8\%$). The ASPERA-3 ion spectrometer (IMA) is mounted on the body of the spacecraft. The instrument itself is a combination of a spherical electrostatic analyzer and a collimator system. Particles are able to enter the instrument within an elevation of ±2°, before electrons are deflected into the spectrometer for analysis, which is conducted using plates of varying voltage to create an energy spectrum (Barabash et al. 2006). Together with the other ASPERA-3 sensors, ELS works toward a more complete understanding of the solar wind–atmospheric coupling at Mars. The IMA is a standalone sensor that contains an electrostatic deflection system, top-hat electrostatic energy analyzer, permanent magnet-based velocity analyzer to separate ion mass, and an MCP detector. The instrument contains 16 anodes that have an azimuthal field of view of 22.°5 and can measure ions per charge to 30 keV q^{-1}.

The MARSIS instrument on Mars Express (Jordan et al. 2009; Orosei et al. 2015) acquires data from altitudes lower than 1200 km. The radar can operate in two different modes, both of which are used in this work. The first mode is the subsurface mode, which is a dual-channel low-frequency sounder and operates at two fixed frequencies to be chosen from 1.8, 3, 4, and 5 MHz. In this mode, the total electron content (TEC) of the entire column of atmosphere can be retrieved from the phase delay that signals suffer when crossing the ionosphere (Sanchez-Cano et al. 2015). The other mode is active ionospheric sounding (AIS), in which the radar sounds the topside ionosphere by doing a sweep of frequencies between 0.1 and 5.5 MHz. In this mode, topside vertical electron density profiles can be retrieved every 7 s.

For our study, we use the ELS and IMA on ASPERA-3 to identify Mars Express crossings of the bow shock and IMB, and MARSIS to look at the behavior of the ionosphere. To avoid any data contamination from the spacecraft itself, we restrict our study to data from ELS anodes 4–11, and IMA anodes to 0–9. These anodes all have unobstructed fields of view. We use the Mars Solar Orbital (MSO) coordinate system, where x is from the center of Mars to the center of the Sun, y is the opposite of the planet's tangential velocity around the Sun, and z completes the right-handed system. We rotate all of our crossing positions by 4° around the Z-axis to account for the solar wind aberration angle, although we acknowledge that this is not always the best angle to use, based on the ranging orbital speed and solar wind speeds. If solar wind velocity varies from 400 to 800 km s^{-1}, and Mars's orbital velocity varies from

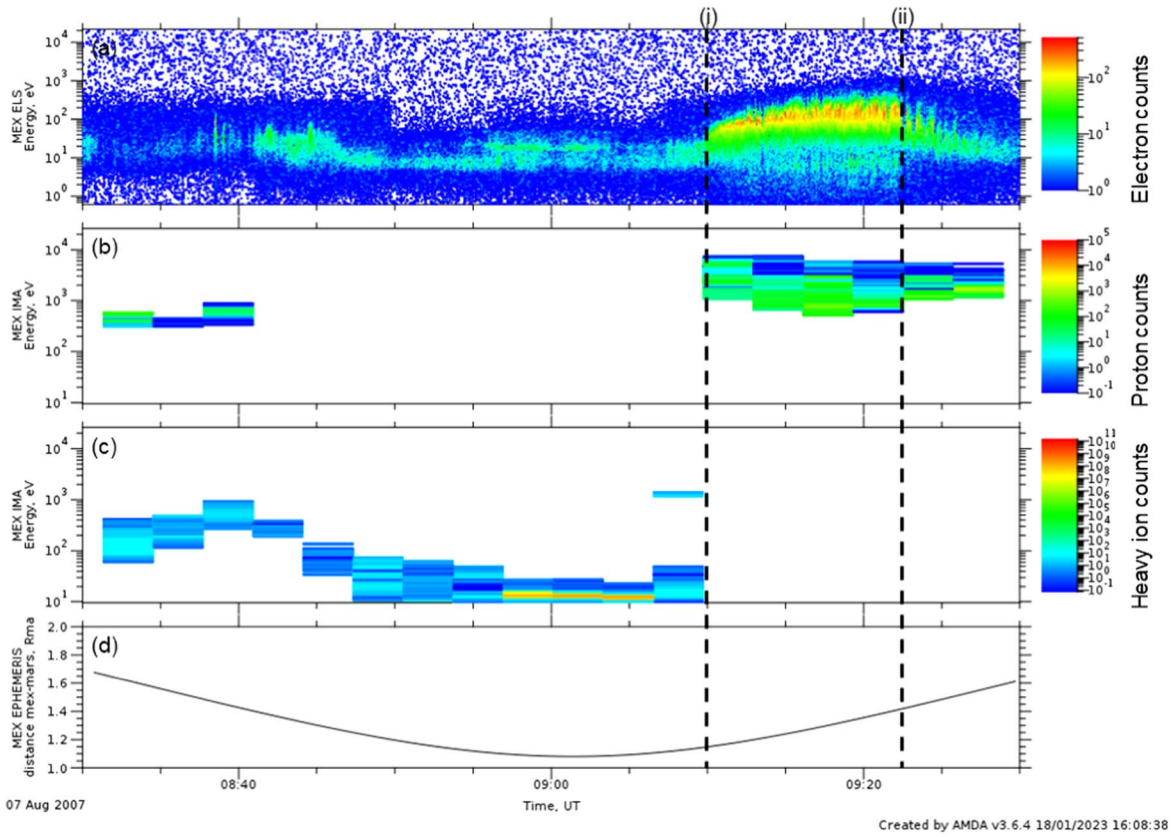

Figure 1. Mars Express ASPERA data from 2007 August 7. Shown here are the (a) electron counts, (b) proton counts, (c) heavy ion counts from the ELS and IMA instruments, and (d) altitude of the spacecraft traveling outbound in it is orbit around Mars. The vertical line (i) indicates an induced magnetospheric boundary (IMB) crossing from the planetary plasma region into the magnetosheath, and (ii) shows a bow shock crossing from the magnetosheath into the solar wind.

21.97 to 26.5 km s^{-1}, then the rotation angle varies from 1°.58 to 3°.8. We use 4° for consistency with other studies.

2.2. Bow Shock Positions

To obtain Mars Express crossings of the bow shock, we used the catalog compiled by Hall et al. (2019). Building on work done by Edberg et al. (2008), Hall et al. (2016, 2019) studied the location of the bow shock over 10 Martian years of data, creating a model that automatically detected a boundary crossing based on observed increases in electron flux. When Mars Express moves from the solar wind into the magnetosheath, there is a sudden increase in electron flux as electrons are heated and density increases at the bow shock (Figure 1(ii)). When the spacecraft moves in the other direction from the magnetosheath into the solar wind, the differential number flux reduces in both magnitude and energy. Hall et al. (2016) created a parameter, *f*, that compounds this information into a singular value. It represents the integrated flux proxy, with units electrons cm^{-2} s^{-1}. If the *f* parameter is enhanced by an order of magnitude in less than five minutes, then a bow shock crossing is encountered. We used this model to obtain bow shock crossings from 2007 May 1 to November 30. We also verified each crossing the model identified by eye, while acknowledging that there may be increased uncertainty when the bow shock crossing occurs in the quasi-parallel sector. This verification is done using electron, proton, and heavy ion data from ASPERA-3. We use the particle counts summed across anodes 4–11 for the electron spectrometer, and anodes 0–9 for the ion mass analyzer to have an unobstructed field of view. Based on the resolution of the electron spectrometer on board Mars Express, along with the uncertainty associated with the spatial scale of the bow shock thickness (Burne et al. 2021), we identify boundary crossings with an uncertainty of ±32 s (Barabash et al. 2006).

2.3. Induced Magnetospheric Boundary Positions

At present, there is no automatic detection algorithm for Mars Express crossings of the IMB. In order to have an accurate catalog of the IMB crossings, we inspected ELS and IMA data for the same study period (2007 May 1–November 30) to identify crossings both in- and outbound. The method to identify an IMB crossing is as follows: when looking for a crossing from inside the IMB into the magnetosheath (outbound), we looked for a sharp increase in the electron energy and counts, the appearance of protons, and the disappearance of heavy ions as we move from planetary plasma into the magnetosheath. We identify the first occurrence of the increase in electron energy as being the IMB. An example outbound crossing can be seen in Figure 1(i). This change occurs over timescales of only 2–3 minutes. The opposite is true for the inbound IMB crossing. During this storm time period, the outbound crossings are easier to identify, due to them occurring on the dayside of Mars, with Mars Express often crossing these boundaries at a nearly perpendicular angle, so a clear change in plasma characteristics is observed. The post-terminator crossings (inbound) at this time are more complex to identify, due to the complexity of the Martian nightside's plasma characteristics, being more irregular with less planetary plasma intensity.

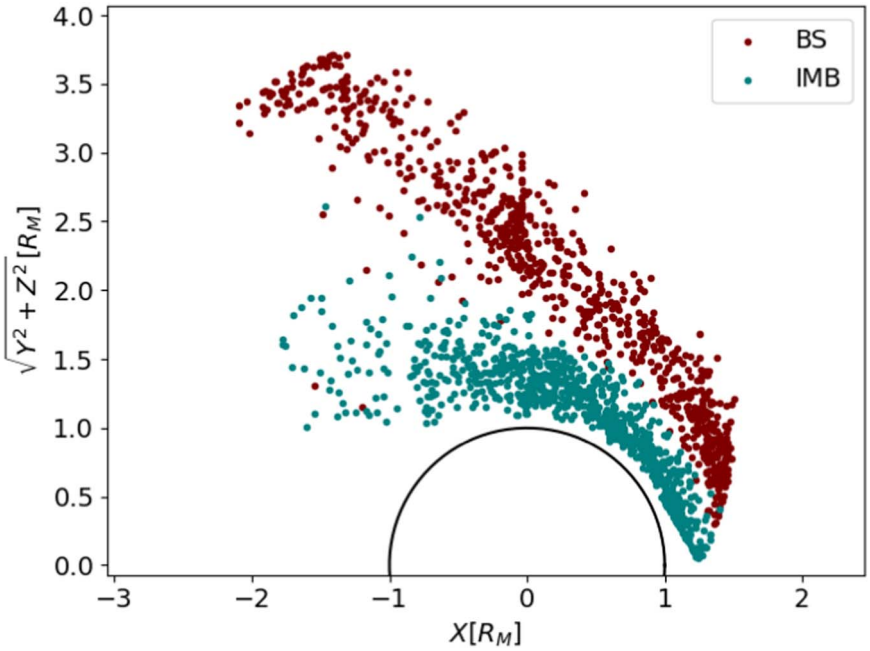

Figure 2. All bow shock (BS, red) and induced magnetospheric boundary (IMB, turquoise) crossings from 2007 May 1 to November 30, as observed by Mars Express. Bow shock positions taken from Hall et al. (2019) and verified by eye. All IMB positions recorded by eye. Plotted in Mars Solar Orbital coordinates.

Moreover, there were some times where either IMA, ELS, or both instruments were turned off. In the cases where one instrument was still on, we attempted to identify boundary crossings if the available data were suitable. Where multiple crossings of the boundary were present, we only considered the first crossing in the time series by Mars Express. Multiple boundary crossings are not something we considered in this study.

2.4. Crossings

Our study period covers 2007 May 1 to November 30. This covers some time before the storm goes global in mid-July and finishes approximately two months after the storm ends in mid-October. In total, we identified 826 bow shock crossings (481 dayside and 345 nightside, where the dayside is $X_{\rm MSO} \geqslant 0$) and 908 IMB crossings (663 dayside and 245 nightside). For most of the study, we only consider dayside crossings, due to the variability in the flaring of the magnetotail on the nightside of Mars. The areographical coverage of all crossings can be seen in the Mars Solar Orbital Coordinates in Figure 2.

In order to investigate the long-term temporal variability of the IMB and the bow shock due to the global dust storm, we must change the form of the data in order to be able to compare crossings without knowing the solar wind parameters. Therefore, we use a 2D model of the boundaries that enables us to compare crossings at fixed points on the surface.

3. 2D Boundary Modeling

In order to compare each boundary crossing, we had to remove variability due to the solar zenith angle (SZA) of the crossing (angle between the Sun's rays and the vertical, where 0° is midday). To do this, we followed an empirical model for each event to identify trends. To look at both boundaries, we used a two-dimensional model following the methodology of Edberg et al. (2008), Vignes et al. (2000), and Trotignon et al. (2006). For each individual boundary crossing, identified using

3. 2D BOUNDARY MODELLING

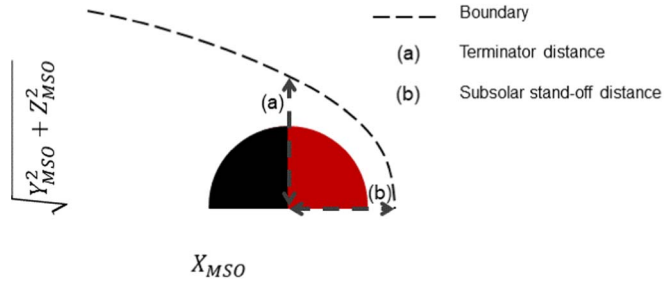

Figure 3. Terminator (a) and subsolar (b) distances, in Mars Solar Orbital Coordinates.

Table 1
Input Parameters from Edberg et al. (2008)

	Eccentricity (e)	Conic Focus (x_0 in $R_{\rm M}$)
Bow Shock	1.05 ± 0.04	0.55 ± 0.12
IMB	0.92 ± 0.03	0.86 ± 0.11

the methods described above, we calculate the subsolar ($R_{\rm SS}$) and the terminator ($R_{\rm TD}$) distances, using Equations (1) and (2), respectively (Figure 3):

$$R_{\rm SS} = x_0 + L(1+e)^{-1} \quad (1)$$

$$R_{\rm TD} = \sqrt{L^2 + (e^2-1)x_0^2 + 2eLx_0}, \quad (2)$$

where $L = r(1 + e\cos\theta)$, and r, θ are the polar coordinates of each boundary crossing, e is the boundary eccentricity, and x_0 is the conic focus.

For both eccentricity and the conic focus, we use the values given in Edberg et al. (2008). These values can be seen in Table 1. This methodology removes the influence of the SZA on the boundary crossings, as they are fitted to the two points

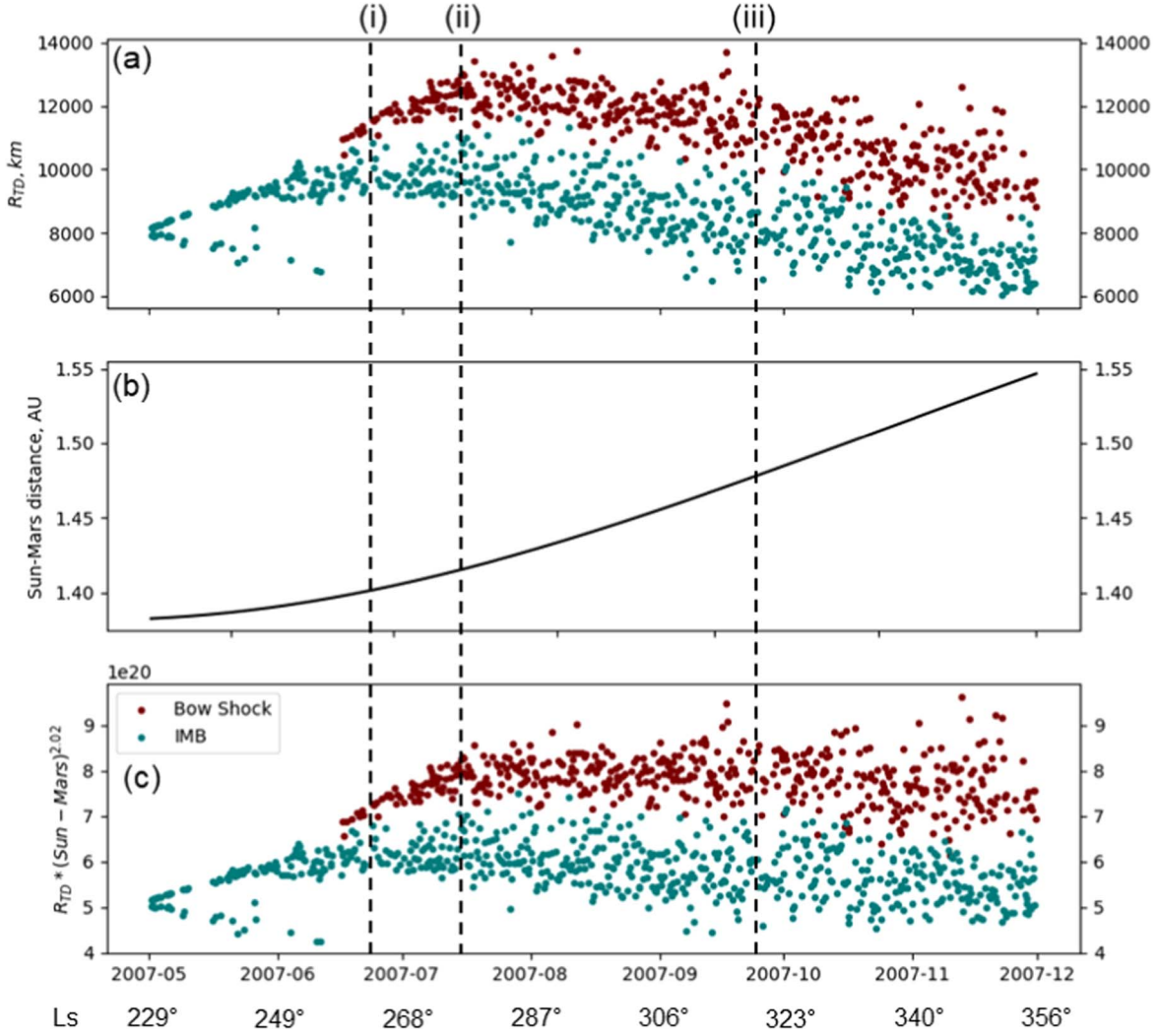

Figure 4. Bow shock and induced magnetospheric boundary terminator distances, calculated for all dayside crossings. All values are from 2007 May 1 to November 30. (a) Terminator distance R_{TD} (see Equation (2)), values given from the center of Mars, (b) Mars–Sun distance during the study period in astronomical unit, (c) normalized terminator distance values. The dust storm phases are marked in the dashed lines: (i) dust loading begins, (ii) dust storm becomes global, and (iii) surface conditions return to normal. The solar longitude of Mars is included on the *x*-axis.

via a conic section. We also removed any variation due to the Sun–Mars distance change by multiplying R_{TD} values by $r^{2.02}$, where r is heliocentric distance, as seen in Figure 4. We assumed a heliocentric distance relationship to the power of 2.02, as estimated by Hall et al. (2016), to model the influence of the dynamic pressure at the Sun–Mars distance. Due to the large number of models available (see discussion in Trotignon et al. 2006) to look at both boundaries, we acknowledge that there are advantages and disadvantages depending on which model is chosen. The Edberg et al. (2008) method was chosen to remove the solar zenith influence, which was very significant when using other model methods.

4. Results

The resulting values for the terminator distance can be seen in Figure 4 for all dayside boundary crossings, with an uncertainty of ±20.4 km for Mars Year 28, taken from Hall et al. (2019). From here on, we only consider this parameter, as the subsolar stand-off distance results for both the bow shock and the IMB provides similar numerical values for both boundaries. We believe this was due to the varying eccentricity and conic foci, in addition to the flaring of the boundaries not being considered. The curvature of the conic section is not fully representative for the shock between shocked and unshocked solar wind at the subsolar point, due to the assumed constant eccentricity and conic focus (Edberg et al. 2009), so modeling the flank is better constrained to represent the boundary. We used eccentricity and conic foci values determined by Edberg et al. (2008). The suitability of these parameters for this data set and others needs to be readdressed, but doing so is beyond the scope of this study. There are no bow shock data points from 2007 May 1 to June 15, due to the orbit of Mars Express being wholly within the magnetosheath at this time. We first observe a crossing of the bow shock by Mars Express on 2007 June 16. We note that the values for the bow shock terminator distances are larger than the averages found in Hall et al. (2016, 2019). This is due to their averages covering over 15 yr of Mars Express data, whereas our values have been calculated for a small subset of data over a few months. We also note that there is an orbital bias present in the data, due to the behavior of Mars Express's orbit (plots of MEx's orbit are shown in the supplementary information; see Figure 13). Before the onset of the storm, the orbit of Mars Express favors the region where

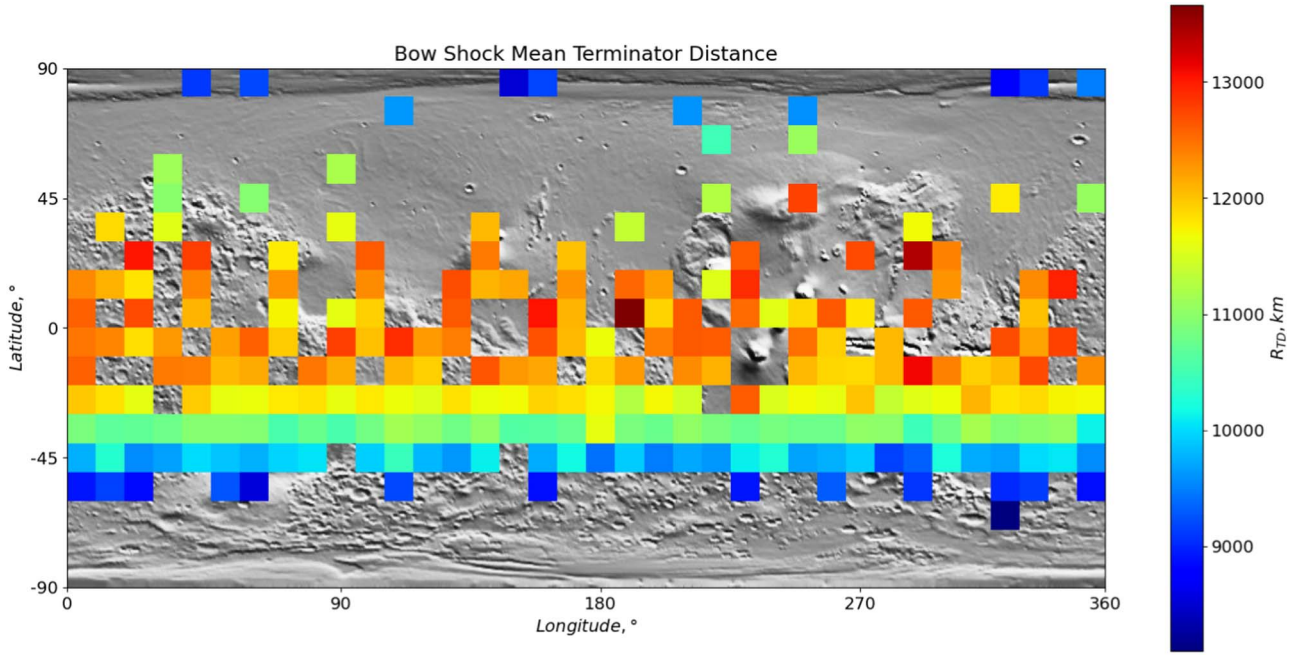

Figure 5. Mean terminator distance of the bow shock calculated per $10^\circ \times 10^\circ$ bin across the Martian surface, for all dayside crossings of the bow shock from 2007 May 1 to November 30. Base map is the Martian topography for reference to surface features. Topography obtained by the digital elevation model of the Mars Global Surveyor's Mars Orbiter Laser Altimeter (USG 2023).

$\sqrt{y^2 + z^2}$ is greater than one, leading to terminator distance values of the IMB being lower (as it is near the subsolar point). This also occurs during perihelion, meaning high values of the terminator distance are unlikely, due both to the orbital bias as well as the expansion of the IMB occurring at perihelion (Brain et al. 2005).

Dust loading at altitude in the atmosphere begins on June 26 (solar longitude L_S 265°) (Fedorova et al. 2018). This is indicated by a vertical line (i) in Figure 4. Prior to this, the terminator distance values for the IMB are mostly clustered in two groups, showing a steady increase in value in one and a decrease in the other. The latter group of crossings are not present when we limit data to an SZA on Mars of the boundary crossing lower than 50°, indicating that these lower terminator values may be due to a different flaring angle of the boundary occurring nearer the nightside of Mars. The bow shock crossings prior to dust loading are also grouped together. Between dust storm onset (i) and the storm going global in extent, at line (ii) in Figure 4, on July 12 (L_S 275°) both data sets begin to show more variability, with data points becoming more scattered. The bow shock still shows an increase in distance, but the IMB begins on average to steadily decrease in distance. Between lines (ii) and (iii) in Figure 4 is the extent of the global storm and decay phase, before surface conditions return to normal on September 25 (L_S 320°–330°). During this time, the average terminator distance for both values show increased variability. This is especially present in the IMB. From September 25 onward, both boundaries show continued scattering of terminator distances when normalized to the solar wind dynamic pressure at the Sun–Mars distance (Figure 4(c)).

We investigate how these values changed based on the areographical position of Mars Express with relation to the surface below for all crossings. To do this, we binned our crossings into $10^\circ \times 10^\circ$ bins along Martian latitude and longitude, and calculated the mean terminator distance for each section across the surface. The results for the bow shock as seen in Figure 5 show the largest mean terminator distance at the equator, with this decreasing toward the north and south poles. There is no obvious trend of mean value with longitude. The IMB (Figure 6) also shows larger values at the equator, with these decreasing toward the south pole. It is difficult to determine how these values vary toward the north pole, due to the lack of coverage. When looking at the variation of values with longitude, however, despite the limitations, the data suggest there is a decrease at middle longitudes, with values of 9000–9500 km from 90° to 270°, and with higher values up to 11,000 km on either side of this region to the west and east. Both sets of results are limited by the number of crossings we have in each bin, which is represented in the supplementary information. Also included in the supplementary information are time splits of Figures 5 and 6, showing the sparsity of the data available when split by storm phase (outlined in Table 4) due to the orbital bias of Mars Express.

5. MARSIS Data Comparison

In addition to looking at the trends over the whole study period, we looked at three Mars Express orbits per storm phase in more detail with data from the MARSIS-AIS instrument. We looked at this to understand the region between the surface and the upper boundaries, to fill in the gap here. These orbits were at different stages of dust storm development, meaning we could obtain ionospheric profiles from MARSIS and compare them during different dust conditions. The orbits are listed in Table 2. These orbits were chosen because they cover similar areographical regions during their orbit (latitudes between −78° and −72°) at similar SZAs (50°–55°), so we can minimize other influences such as areographical position or SZA, potentially uncovering the signatures of the dust. We also looked at the TEC during the dust storm, and found no significant variation. The topside electron density profiles are fitted with the Chapman function, which describes the main

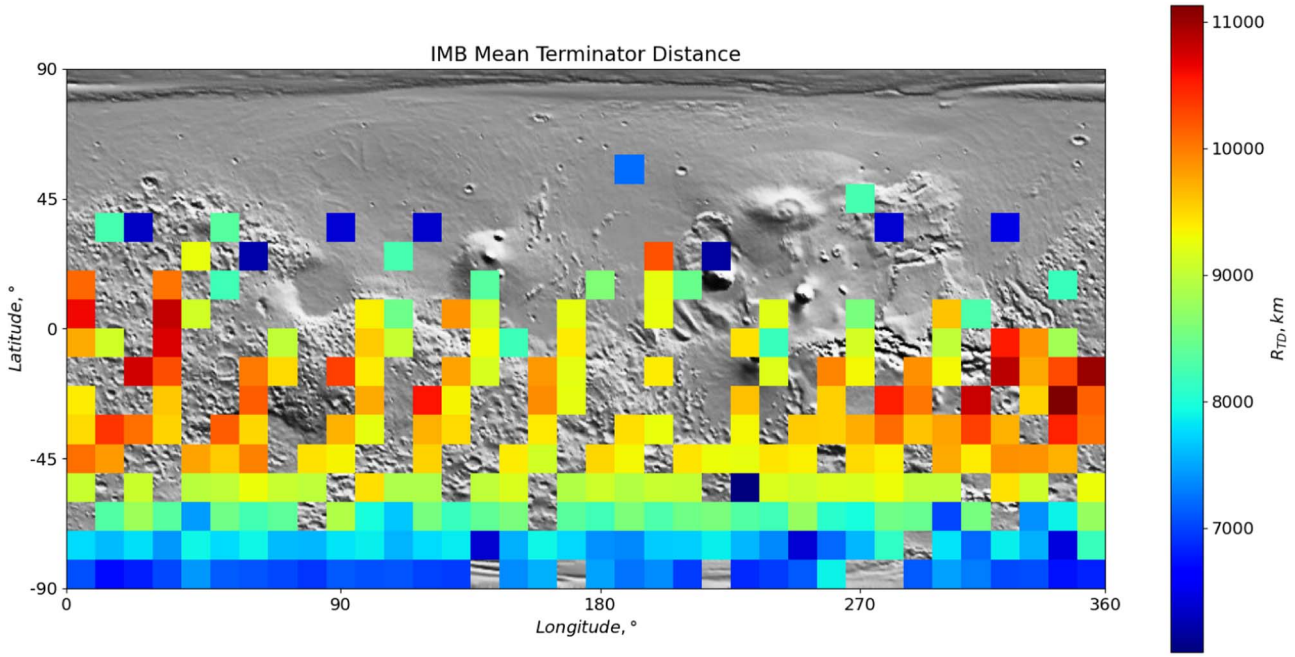

Figure 6. Mean terminator distance of the induced magnetospheric boundary calculated per 10° × 10° bin across the Martian surface, for all dayside crossings of the IMB from 2007 May 1 to November 30. Base map is the Martian topography for reference to surface features. Topography obtained by the digital elevation model of the Mars Global Surveyor's Mars Orbiter Laser Altimeter (USG 2023).

Table 2
Mars Express Orbits Used for MARSIS Ionosphere Analysis

Label	Orbit Number	Time	H_{max}, km	TEC, e+15	N_0, e+11 m^{-3}	Altitude of N_0, km
Before global storm	4359	May 28 06:09	8.69	6.63	1.93	150
	4360	May 28 12:52	10.68	6.40	1.94	143
	4361	May 28 19:35	9.73	6.31	1.99	138
Start of global storm	4465	Jun 26 22:28	8.78	5.87	1.97	146
	4467	Jun 27 11:54	11.39	5.44	1.92	141
	4469	Jun 28 01:21	11.56	6.74	1.77	140
Global storm	4579	Jul 28 20:33	9.94	6.37	1.98	141
	4580	Jul 29 03:16	10.26	6.70	1.89	154
	4582	Jul 29 16:42	11.79	6.83	1.89	142

Notes. H_{max}: the neutral scale height at the peak of the ionosphere from Chapman fits. TEC: total electron content. N_0: peak electron density at solar zenith angle = 0°.

layer of the Martian dayside ionosphere. The neutral, atmospheric scale height was introduced in the Chapman function to vary linearly with altitude (Sánchez-Cano et al. 2013) in order for it to better describe the topside electron density profiles at Mars. The fit of the Chapman layer to the electron density profiles was achieved by using a least-squares curve-fitting method.

The ionospheric profiles produced from sample orbits between orbits 4365 and 4569 (Figure 7) show no variation in the ionospheric peak electron density or overall profiles due to the onset of the global dust storms. There is, however, variation with altitude during the global storm (4579–4582): the electron density is higher at altitudes between 300 and 450 km than at other times. This is not seen in the profiles prior to the storm and at the start of the global storm. The neutral scale heights from the Chapman fits show a slight increase in median values when the global storm begins, indicating that the atmosphere may be lifted. It is difficult to conclude if this is happening, as we are only looking at nine orbits. Further study of more ionospheric profiles at different dust phases would improve our understanding.

6. Discussion

6.1. Bow Shock

In previous studies (Vignes et al. 2000; Trotignon et al. 2006; Edberg et al. 2008; Bertucci et al. 2011; Hall et al. 2016, 2019), the position of the bow shock was found to vary significantly over the solar cycle (7%) and a Martian year (11%). This is mainly due to variations in the solar wind conditions—the environment external to the induced magnetosphere of Mars due to varying EUV flux. At present, there are no conclusive results showing that atmospheric effects at Mars have an influence on the bow shock position. Figure 4 shows that the onset of the global dust storm at Mars coincides with increased variability of the calculated distance from the center of Mars to where the bow shock crosses the terminator (the terminator distance). Due to the lack of Mars Express orbital

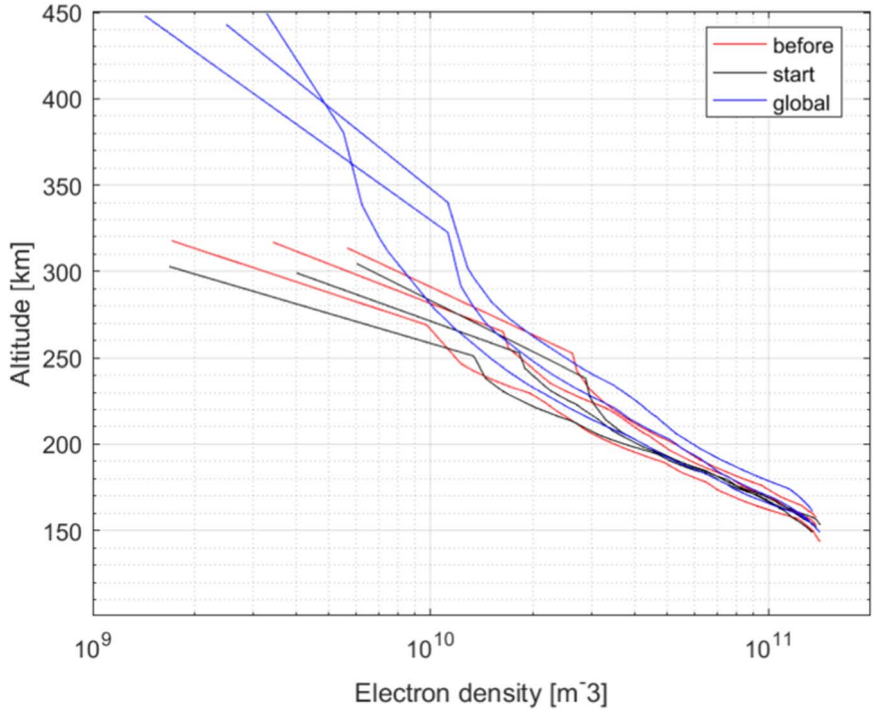

Figure 7. Ionosphere profile for electron density, calculated from MARSIS data. Colors indicate different dust storm phases, with red being the pre-global dust storm (May 29), black the start of the global storm (June 29), and blue during the global dust storm (July 29).

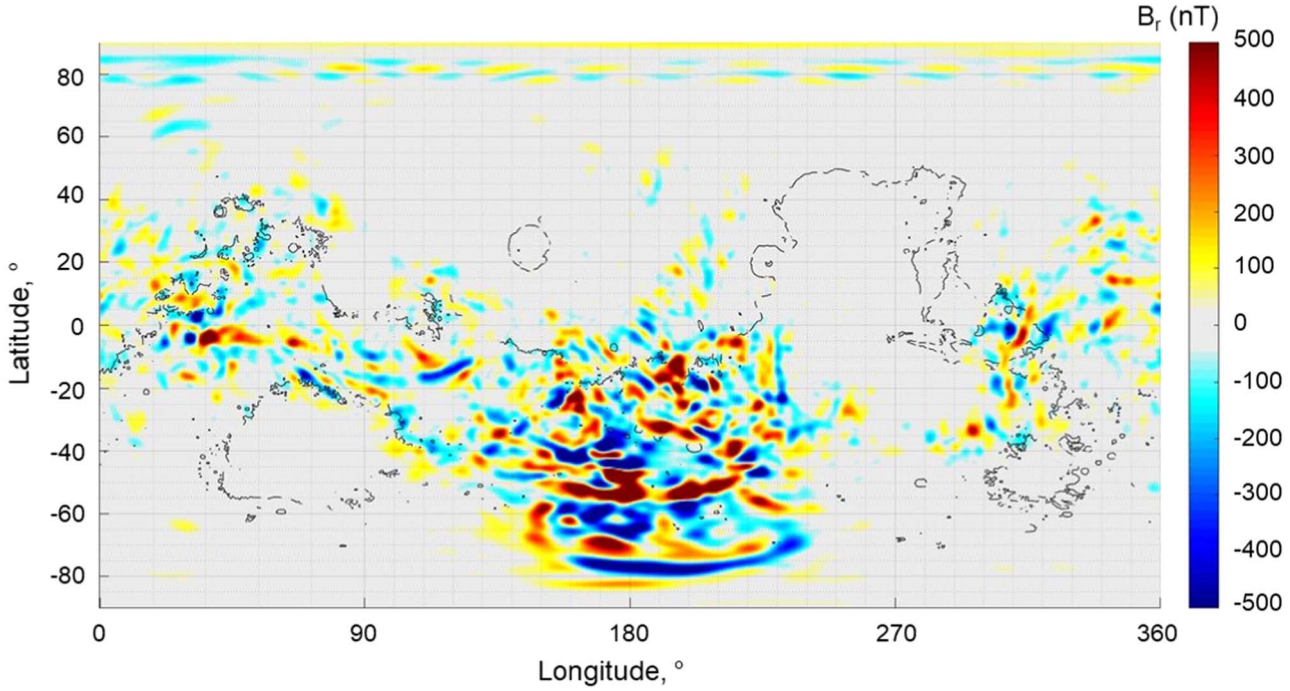

Figure 8. Radial crustal magnetic field strength from the G110 model at 120 km altitude, taken from Gao et al. (2021).

coverage of bow shock crossings before dust begins to load the atmosphere, it is not clear whether the bow shock terminator distance was more stable before the dust storm. In addition, the orbit of Mars Express favors the equatorial region during the storm duration, and the southern hemisphere after the storm ends, as shown in the supplementary information, meaning our results are inconclusive.

The influence of the crustal magnetic fields (Figure 8) on the bow shock is complex, with studies from Edberg et al. (2008) indicating a north/south variation in location, with the boundary being farther from the surface in the southern hemisphere. Gruesbeck et al. (2018) identified that the effect of crustal fields on the bow shock also depends on their relative local time. Garnier et al. (2022b) highlighted that coupling between the ionosphere and the IMF on the bow shock appears to be seasonal and correlated with the TEC. We also acknowledge that crustal field orientation plays a role in boundary location (Gruesbeck et al. 2018; Garnier et al.

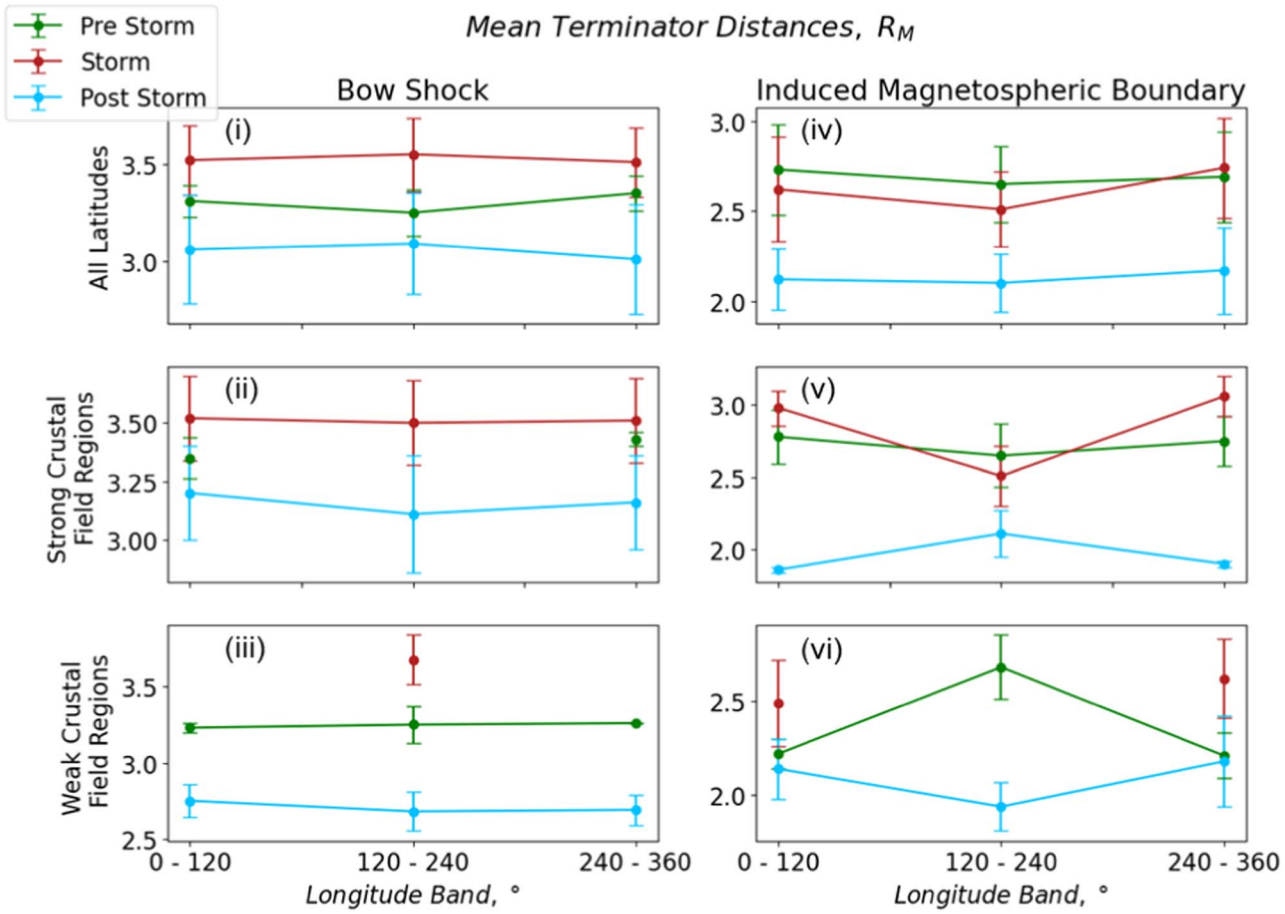

Figure 9. Mean terminator distances for the bow shock ((i), (ii), and (iii)) and the induced magnetospheric boundary ((iv), (v), and (vi)) for all dayside crossings from 2007 May 1 to November 30. Values have been split into three longitude bands for 0°–120°, 120°–240°, and 240°–360°, and the mean value has been calculated for all crossings within each longitude band. (i) and (iv) are mean values for all latitudes within the band split, (ii) and (v) are for the areas defined as having "strong" crustal magnetic fields (see Table 3) in each band split, and (iii) and (vi) are regions with "weak" crustal magnetic fields. Green points are for boundary crossings before the global dust storm, red are for the peak and decay phases of the storm, and blue shows data after the global dust storm has ended (Table 4). Boundary positions are calculated by using the 2D model.

2022b), but it is beyond the scope of this project to consider. Our results (Figure 5) show no strong link between the bow shock terminator distance and the location of the crustal magnetic fields. This may be due to the dust storm hiding or shielding the effect of the crustal magnetic field on the bow shock, which is discussed more in our analysis of the IMB results. Here, we have the largest values for the terminator distance occurring $\pm 20^{\circ}$ in latitude. Values then decrease as latitude increases to the poles. We also split Mars into three longitudinal bands, and split the bands into areas of low and high crustal magnetic fields, following Edberg et al. (2008). These results can be seen in Figures 9(i)–(iii). When looking at the split between different dust phases, represented by the different colors, the terminator distance has its highest values during the global dust storm period, with the mean value decreasing during the post-dust-storm phase for all data splits. The terminator distance values do not differ significantly based on the areographical position of the crossing.

6.2. Induced Magnetospheric Boundary

Moving now to the potential impact of the dust storm, we note that Figure 4 shows that, before dust loading begins and the storm goes global at times (i) and (ii), the calculated terminator distance for IMB crossings on the dayside is grouped closer together and shows an upward trend. As the dust storm develops and eventually goes global, the boundary location becomes more variable, with terminator distances becoming more varied from July onward. This is likely due to the amount of dust lifted into the atmosphere varying with location during the development of the storm, meaning the IMB will vary in position with the crossing location with respect to the surface and the storm development at that point.

The IMB can bulge outward over areas of crustal magnetic fields, due to the increased ionospheric pressure there from trapped planetary plasma (Crider et al. 2002, 2003). It is therefore reasonable to expect to see this in our data, shown in Figure 6. When looking at the mean terminator distance in each bin, we actually see a dip in values over areas of strong crustal fields at the middle longitudes, with values increasing away from this region at the same latitude. This is the opposite of what is expected. We followed the Edberg et al. (2008) method and split the globe into longitudinal bands and split each band into areas of strong and weak crustal fields (Table 3), to look at the terminator distance during different storm phases (Table 4). The results can be seen in Figures 9(iv)–(vi). It is clear in (v) that there is a dip in the terminator distance, during the global dust storm (red line) over the longitude band of 120°–240°, over strong crustal magnetic fields. After the storm ends, this bulge over this longitude bands returns, as the blue line

Table 3
Areas of Strong and Weak Crustal Magnetic Fields for Three Longitude Bands of Mars

Longitude Band	0°–120°	120°–240°	240°–360°
Strong Crustal Field Latitudes	−45°–45°	−90°–0°	−45°–45°
Weak Crustal Field Latitudes	$< -45°, > 45°$	0°–90°	$< -45°, > 45°$

Note. Defined by Edberg et al. (2008) and used for statistical analysis.

Table 4
2007 Global Dust Storm Development Split into Sections for Statistical Analysis of Results Before, During, and After the Event

2007 Dates	Dust Storm Phase
May 1–Jun 25	Before Global Dust Storm
Jun 26–Sep 25	Global Storm and Decay Phase
Sep 25–Nov 30	After Global Dust Storm

increases. These results do not show any direct influence over the strong crustal fields before the storm, which is different from previous studies. This may be due to the orbit of Mars Express not favoring the southern hemisphere before the storm, introducing a bias into the data coverage (shown in Appendix Figures 13 and 14).

Crustal magnetic fields are known to trap the planetary plasma, and Fang et al. (2017) found a shielding effect for atmosphere loss occurring over crustal fields. We suggest that, over crustal fields, the confinement of charged particles here leads to lower rates of ionization compared to elsewhere on the planet. We visualize this process in Figure 10. The uplift of dust, aerosols, and atmospheric particles across the globe enhances mixing with charged particles, leading to photo-dissociation of H and O, increasing atmospheric escape (Chaffin et al. 2021). However, the amount of charged particles available for this process is limited over crustal fields due to the confinement by the crustal fields, meaning there is not as much pressure from the ionosphere to the magnetosheath here in comparison with other areas of the surface.

6.3. Ionospheric Signatures

To investigate signatures in the ionosphere, we examined data from MARSIS-AIS and created ionospheric profiles. We used the Chapman model to examine the TEC and the neutral scale height, and further examined 3D MHD models (see Appendix A2) to look at how a dusty scenario may vary from where the boundaries are expected to be positioned (based on modeled solar wind input).

The ionospheric profiles provided by MARSIS indicate that, during these orbits, there is little variation in the ionospheric peak due to the dust conditions. This is different to previous studies, which find that dust storms raise the ionospheric peak (Qin et al. 2019; Fang et al. 2020; Felici et al. 2020). However, the profiles obtained during the global dust event suggest that there are higher densities of electrons at altitudes of 300 km and above, which may be due to the uplift of dust. We have also looked at the TEC observations from MARSIS-subsurface during this period. Although not shown in here, no significant variations were found in the total atmospheric column of electrons (from surface to spacecraft) during the storm. This indicates that no enhancement of ionization occurs, but as suggested by MARSIS-AIS, electrons were lifted to higher altitudes. The ionosphere is more sensitive than the higher-altitude boundaries to atmospheric changes on Mars, and although there were no obvious variations in the electron peak density of the ionosphere during the dust storms (Figure 7), there may still be a signature of the storm in the IMB location.

7. Conclusions

We have used 2D empirical models to investigate whether the 2007 global dust storm at Mars influenced the location of the bow shock and IMB. The bow shock showed no strong trend in location due to the onset and development of the global dust storm, but did show an increased variability in the boundary's position during the storm, meaning the boundary location was not constant over time. Unfortunately, as we did not have bow shock crossings leading up to the storm, we could not determine if this was directly linked to the dust storm. This study found no observable correlation between the bow shock location and the locations of crustal magnetic fields regions; this is most likely to be hidden behind other drivers such as the magnetosonic Mach number, which we cannot determine with Mars Express data, in addition to the Mars Express orbit favoring the equatorial band during the event introducing an orbital bias. We acknowledge that solar EUV may also be influencing the data, but we have looked at the F10.7 flux and found that they do not indicate an influence on our results. Previous work (Edberg et al. 2008; Fang et al. 2017; Gruesbeck et al. 2018; Garnier et al. 2022a, 2022b) observed that the bow shock bulges over the southern hemisphere due to the crustal fields, but did not consider only times of dust events on Mars.

For the IMB, we do have data before the storm that may indicate a clearer direct link to the storm's onset. The IMB showed that the onset of the storm coincided with more scattering and variability in the boundary location, meaning the boundary's altitude with respect to the surface varied over our study. In addition, when comparing to crustal field location, the boundary seemed to dip over these areas, despite orbital limitations, which is the opposite of what has been found in previous studies that did not consider dust scenarios. We suggest that this could be due to the trapping of the planetary plasma reducing the rate of reactions between dust and atmospheric particles, meaning that there is a pressure imbalance here when compared to other areas of the surface.

Many studies have been done to investigate how the IMB and bow shock vary over time and find variations due to crustal magnetic fields (Edberg et al. 2008; Fang et al. 2017; Garnier et al. 2022a, 2022b) and solar conditions (Edberg et al. 2008; Gruesbeck et al. 2018; Hall et al. 2019; Wang et al. 2020, 2021), and they have found that boundaries are farther from the surface over crustal magnetic fields and low solar wind conditions (or at solar minimum). These studies often cover multiple years worth of data, so the dust season is not

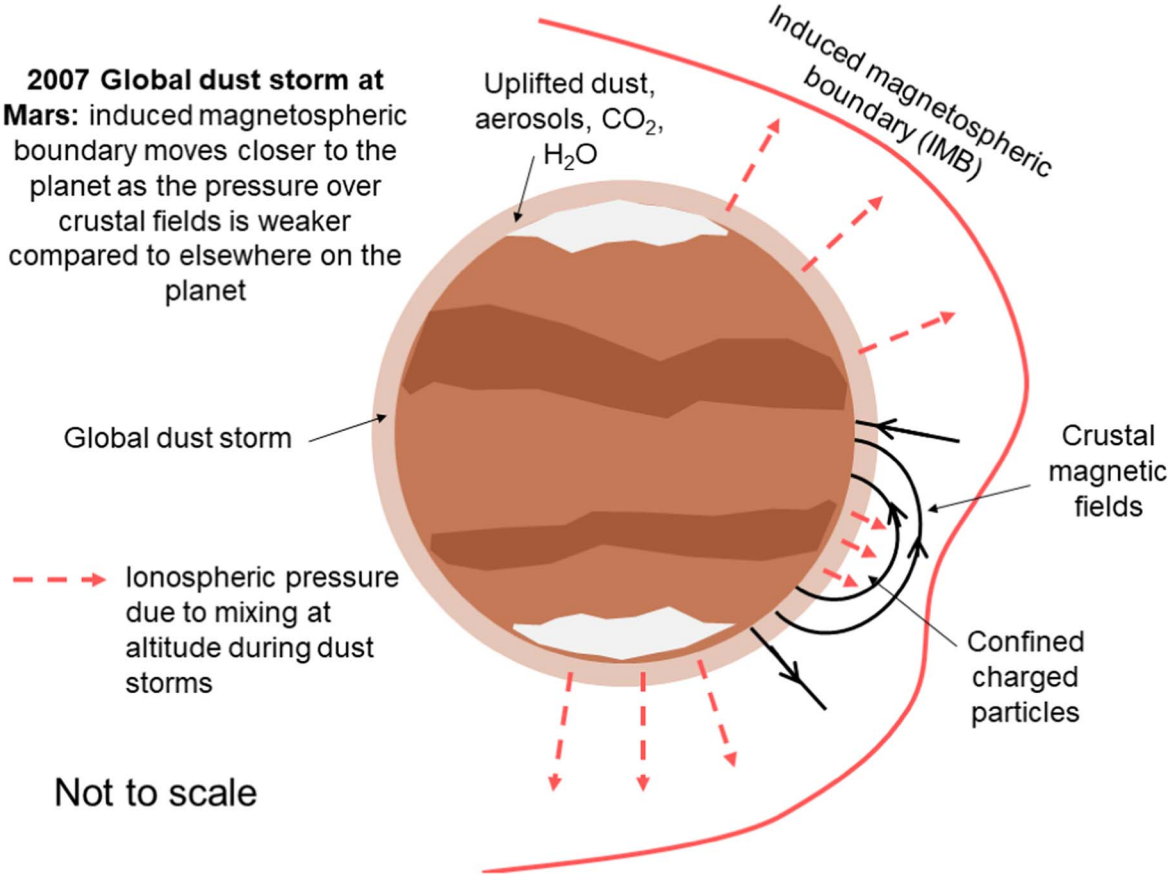

Figure 10. Potential causes of the depression in the induced magnetospheric boundary over crustal fields found in the 2007 global dust storm. Not to scale.

excluded from these results. Our study looks specifically at the dust storm season for the first time.

We also investigate ionospheric profiles from MARSIS during the development and start of the global storm and find no conclusive link between changes in TEC and the dust storm phase. However, electrons were lifted to higher altitudes, although no enhancement of ionization occurs.

Further work is underway on the study of global dust storms, with the 2018 (Mars Year 34) global dust storm having data from both Mars Express and MAVEN. This will provide more data to understand how different areas of the magnetosphere may be affected during dust events. In addition, comparing a global dust storm to normal, calm conditions at a similar solar longitude may also help eliminate other causes of these results.

Acknowledgments

Data analysis was performed with the AMDA science analysis system provided by the Centre de Données de la Physique des Plasmas (CDPP) supported by CNRS, CNES, Observatoire de Paris, and Université Paul Sabatier, Toulouse. Simulation results have been provided by the Community Coordinated Modeling Center (CCMC) at Goddard Space Flight Center through their publicly available simulation services (https://ccmc.gsfc.nasa.gov). The ENLIL Model was developed by the Dusan Odstricil at the University of Colorado at Boulder. C.E.R. acknowledges support from STFC studentships ST/S50578X/1, and ST/V507155/1. A.J.C., A. W., and G.H.J. acknowledge support from STFC grants ST/S000240/1 and ST/W001004/1. R.H. acknowledges support from STFC studentship 2062537. Research by G.H.J. was supported through the Visiting Scientist program of the International Space Science Institute (ISSI) in Bern. B.S.-C. acknowledges support through STFC Ernest Rutherford Fellowship ST/V004115/1, M.L. through STFC grant ST/W00089X/1, and D.M. from a PhD Studentship supported via the University of Leicester's Future-100 Scholarship scheme.

Appendix
Supplementary Information

Figures 11 and 12 illustrate the counts per latitude and longitude bin for calculations used in Figures 5 and 6.

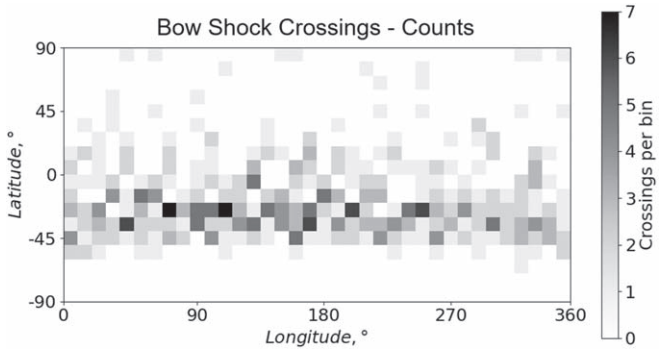

Figure 11. Number of bow shock crossings per bin used in Figure 5.

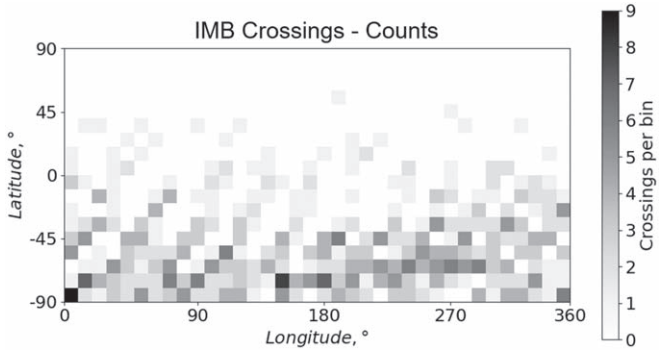

Figure 12. Number of induced magnetospheric boundary crossings per bin used in Figure 6.

A.1. Mars Express Orbital Limitations

Figures 13 and 14 show the Mars Express orbital limitations resulting in sparse data coverage when separated into time splits over the study period. Figure 13 shows the Mars Express orbit and Figure 14 shows the geographical coverage of Mars Express in different dust phases

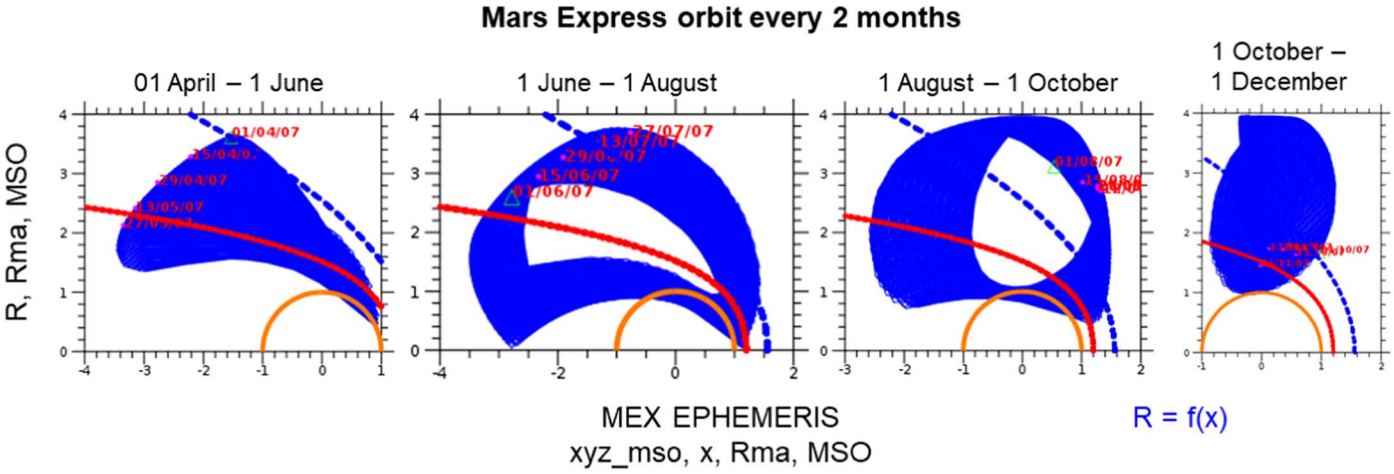

Figure 13. Orbit of Mars Express in Mars Solar Orbital coordinates in two-month intervals from 2007 April to December.

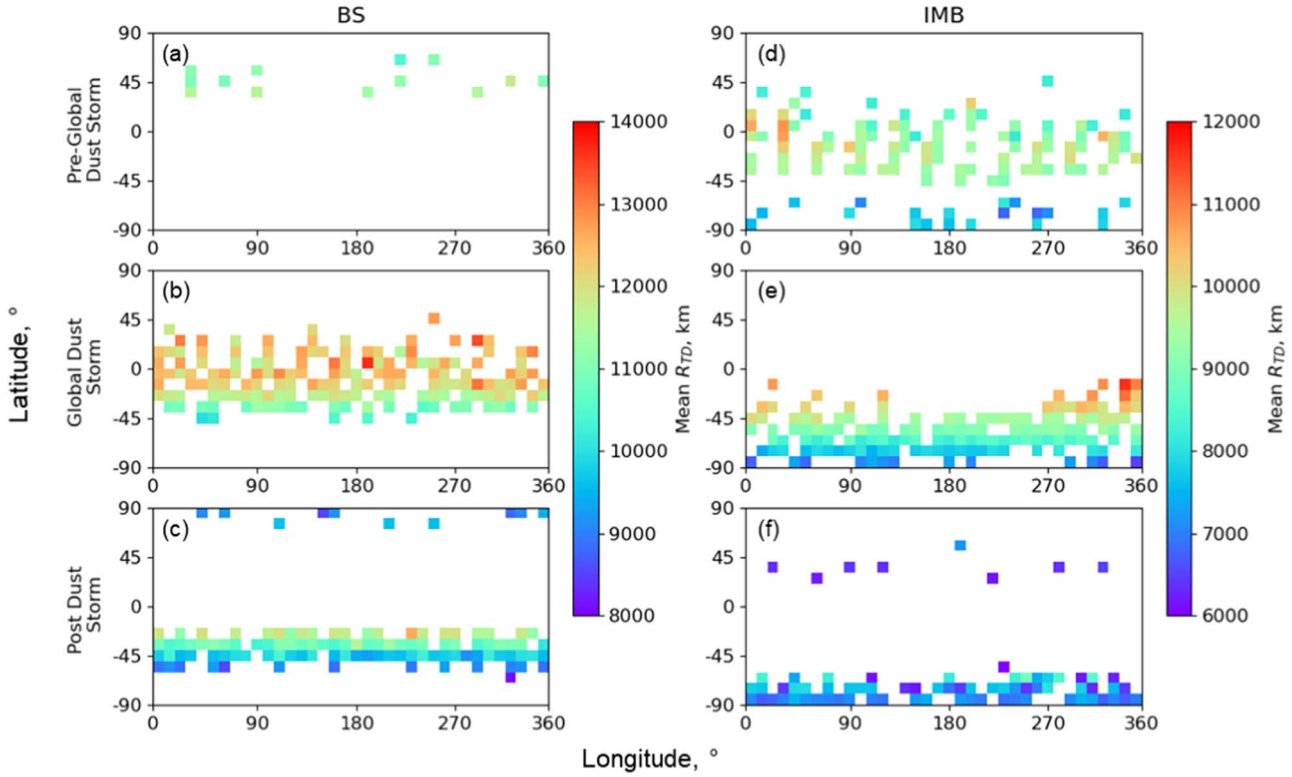

Figure 14. Mean terminator distances per 10° × 10° bin for the bow shock (a)–(c) and the induced magnetospheric boundary (d)–(f), split by storm phase outlined in Table 4.

A.2. 3D Boundary Modeling

To also consider the influence of varying solar wind conditions, we looked at 3D MHD models that include the bow shock based on the work of Wang et al. (2020). With given solar wind conditions (density, velocity, and dynamic pressure), they provide parameter values for subsolar stand-off distance r_0, eccentricity ϵ, degree of flaring α_0, elongation degree α_1, north–south asymmetry α_2, dawn–dusk asymmetry α_3, and twisting angle ω. This model does not have any input linked to the dust conditions on the surface, so it produces the expected boundary surface based on the solar wind conditions at the time. This means we can compare the crossings of Mars Express with the model during different stages of dust development

$$r = r_0\left(\frac{1.0+\epsilon}{1.0+\epsilon\cos\theta}\right)^{\alpha_0+\alpha_1\cos[2(\phi-\omega)]+\alpha_2\cos\phi+\alpha_3\sin\phi}. \quad \text{(A1)}$$

For each of our bow shock and IMB crossings, we convert the MSO coordinates to polar coordinates (r, θ, ϕ) and then produce a boundary surface in three dimensions in MSO coordinates using Equation (A1). We use the same equation for both boundary surfaces, but use differing values for the eccentricity and conic focus given in Table 1. We then compare the position of the Mars Express crossing of the boundary to the modeled boundary surface, and calculate the closest distance between the two. A schematic of this distance can be seen in Figure 15.

A.2.1. Solar Wind Data

To obtain the parameters provided by Wang et al. (2020), we needed to obtain data for the solar wind conditions during our study period. Unfortunately, for the first part of our study period, Mars Express's orbit is within the magnetosheath and does not cross the bow shock. This means we do not have consistent solar wind data measured by ASPERA for our study period. Because of this, we looked at two solar wind propagation models to use as our initial input into the Wang model.

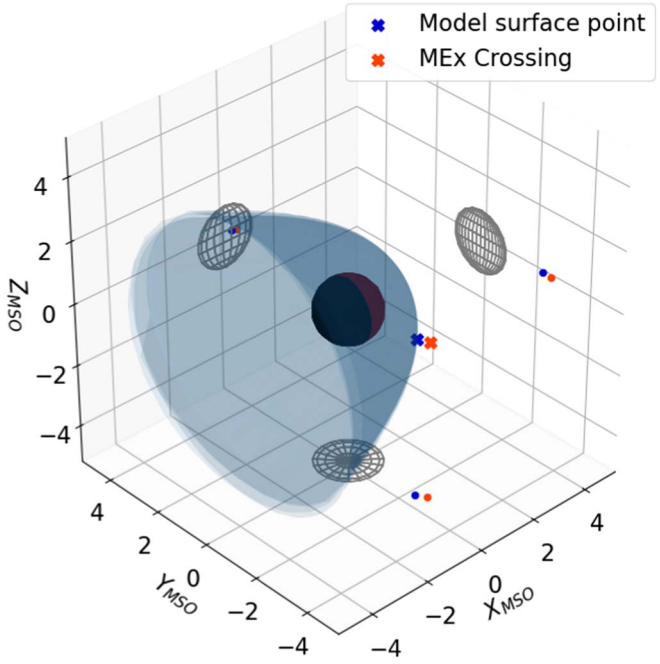

Figure 15. Bow shock surface in Mars Solar Orbital coordinates, produced by the Wang et al. (2020) model with solar wind input from the Tao model. Model produced for conditions at the time of the Mars Express crossing of the boundary at 20:49:24 on 2007 November 12. Blue cross is the point on the model boundary surface that is closest to the Mars Express crossing (orange cross). Points projected to each axis are represented by dots.

Figure 16 shows a comparison between the two different solar wind propagation models (along with the ASPERA solar wind data, plotted in red, when available). These two models are the ENLIL and Tao models. The ENLIL model (Odstrcil 2003) provided by the Community Coordinated Modeling Center is a 3D magnetohydrodynamical model of the heliosphere, based on boundary conditions (Carrington Rotations 2056–2063). This model showed many differences from the ASPERA data, whereas the Tao model (Tao et al. 2005, 2015) overall provided a good match with ASPERA

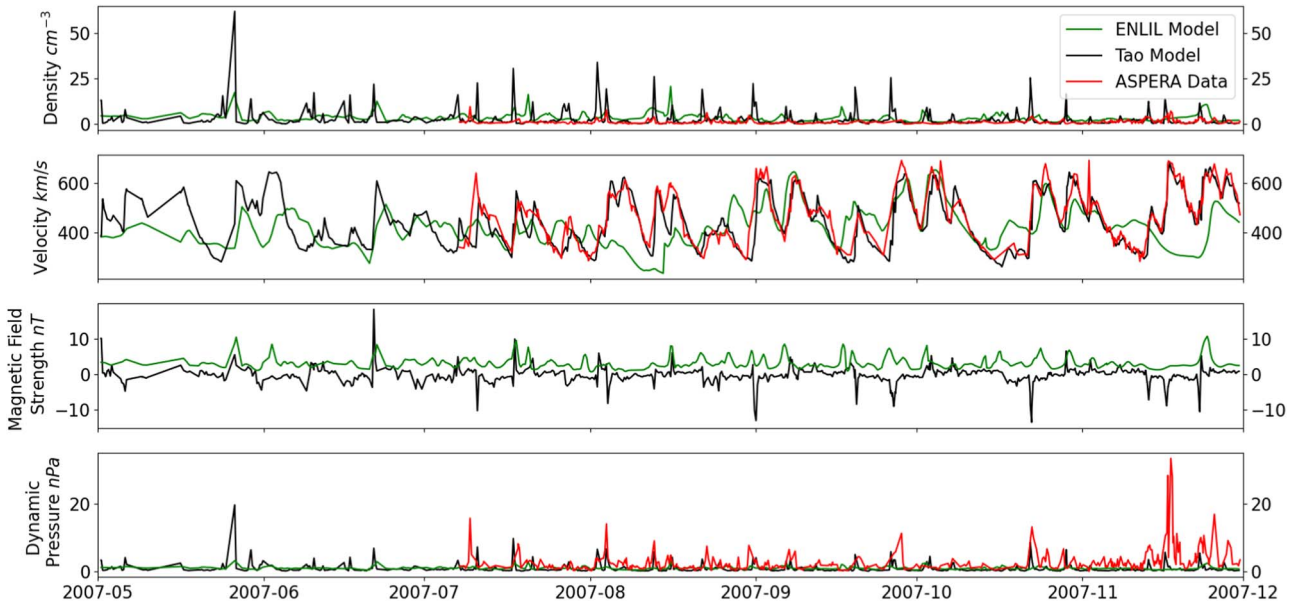

Figure 16. Comparison of the ENLIL and Tao solar wind models to the ASPERA solar wind data at Mars.

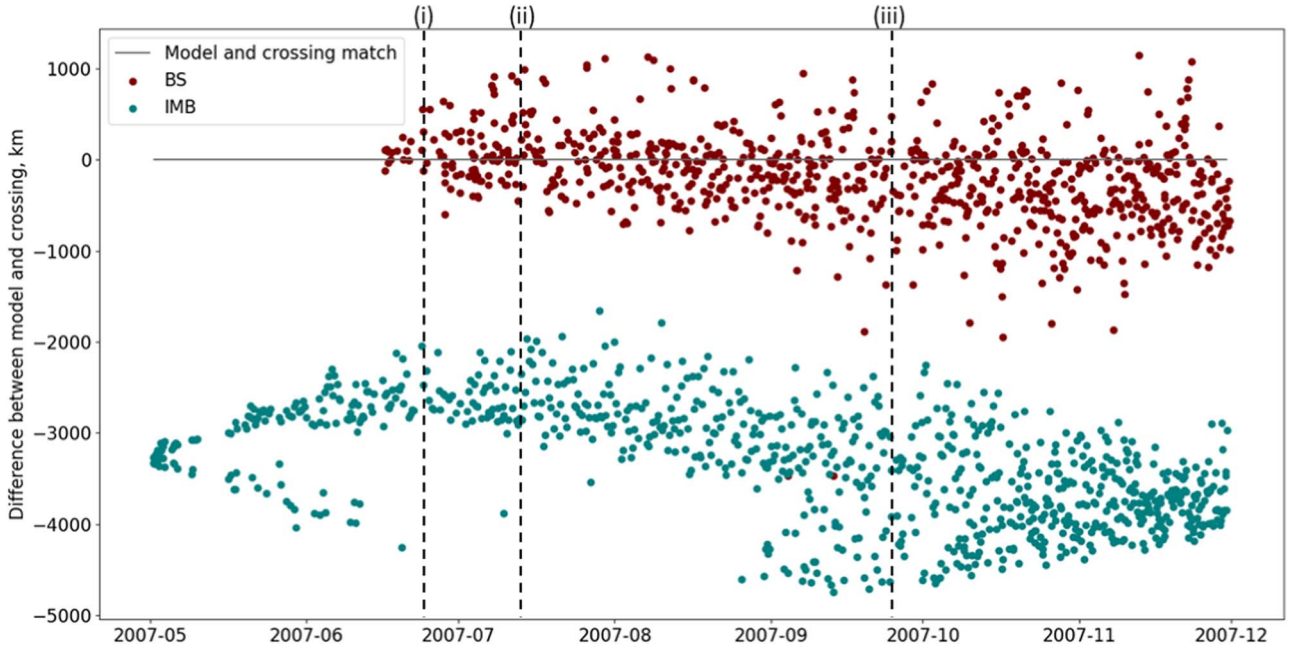

Figure 17. Differences between the Wang et al. (2020) model boundary location and the Mars Express crossing of the boundary. Gray line indicates that the Mars Express crossing matched where the model predicts the boundary to be, located using the solar wind conditions from the Tao model. Black dashed lines indicate different dust stages: (i) dust loading begins, (ii) dust storm becomes global, and (iii) surface conditions return to normal. Maroon and teal points represent the bow shock and induced magnetospheric boundary, respectively. The plot includes all dayside and nightside crossings of boundaries.

data, in particular for the velocity, although several spikes in density are not produced by the model. The Tao model uses simulation outputs from solar wind parameters observed at Earth by the STEREO-A and STEREO-B spacecraft, propagated to Mars using a 1D MHD model. Consequently, we chose to use the Tao solar wind model as our input to the Wang model.

A.2.2. Results

Figure 17 shows the difference between the Wang et al. (2020) MHD model position of each boundary, and the Mars Express crossing of the boundary. A value of 0 would mean the model and the crossing are exactly the same, positive values would indicate the Mars Express crossing shows the boundary is further from Mars than the model predicts, and negative values show the opposite. For the bow shock, results begin roughly centered around 0, but as time goes on, the scatter in the results increases with a slight negative trend, indicating that the Mars Express crossings were closer to the planet during the global dust storm than the model predicts. The Wang model predicts the bow shock location based on the solar wind conditions inputted from the Tao model, and it does not consider dust in its predictions. The results here indicate the dust storm is causing the boundary to be closer to the surface than it would be in a non-dusty scenario. For the IMB, all results are negative, indicating the boundary is seen to be closer to Mars than the Wang model predicts. After the dust storm becomes global, there is greater scatter in the estimates of the IMB, with negative difference values increasing in magnitude from mid-August onward. At the beginning and end of the study, there seem to be two branches of data. The branches away from the main data group are where we have data from the dawn and dusk sides of Mars.

A.2.3. Discussion

The 3D model produced by Wang et al. (2020) takes the solar wind conditions at Mars as a key input; the solar wind is known to influence the location of the IMB and the bow shock. The 2D model does not account for this variability. Although the Wang model combined with data propagated using the Tao technique is a good match with the ASPERA observations available, it is not perfect and we are unable to compare it to the solar wind at the start of the study, due to orbital constraints of Mars Express. In addition, when plotting the 3D results, there is a strong correlation between the differences in boundary position and the SZA of the crossings, which we cannot remove. For these reasons, we focus the rest of the analysis on the results from the 2D model. For both models, we acknowledge that it would be useful to compare the results with the previous and later Mars years (27 and 29), but this is beyond the scope of this study.

ORCID iDs

Catherine E. Regan https://orcid.org/0000-0001-8784-5919
Andrew J. Coates https://orcid.org/0000-0002-6185-3125
Geraint H. Jones https://orcid.org/0000-0002-5859-1136
Beatriz Sánchez-Cano https://orcid.org/0000-0003-0277-3253
Richard P. Haythornthwaite https://orcid.org/0000-0002-5836-2827
Mats Holmström https://orcid.org/0000-0001-5494-5374

References

Acuna, M. H., Connerney, J. E. P., Wasilewski, P., et al. 1998, Sci, 279, 1676
Barabash, S., Lundin, R., Andersson, H., et al. 2006, SSRv, 126, 113
Barlow, N. G. 2008, Mars: An Introduction to its Interior, Surface and Atmosphere (Cambridge: Cambridge Univ. Press)
Bertucci, C., Duru, F., Edberg, N., et al. 2011, SSRv, 162, 113
Bertucci, C., Romanelli, N., Chaufray, J. Y., et al. 2013, GeoRL, 40, 3809

Bhattacharyya, D., Clarke, J. T., Bertaux, J. L., Chaufray, J. Y., & Mayyasi, M. 2015, GeoRL, 42, 8678
Brain, D. A., Halekas, J. S., Lillis, R., et al. 2005, GeoRL, 32, L18203
Burne, S., Bertucci, C., Mazelle, C., et al. 2021, JGRA, 126, e28938
Chaffin, M. S., Kass, D. M., Aoki, S., et al. 2021, NatAs, 5, 1036
Chaufray, J. Y., Gonzalez-Galindo, F., Lopez-Valverde, M. A., et al. 2021, Icar, 353, 113498
Connerney, J. E., Acuna, M. H., Wasilewski, P. J., et al. 2001, GeoRL, 28, 4015
Crider, D. H., Acuña, M. H., Connerney, J. E., et al. 2002, GeoRL, 29, 1170
Crider, D. H., Vignes, D., Krymskii, A. M., et al. 2003, JGRA, 108, 1461
Duru, F., Baker, N., De Boer, M., et al. 2020, JGRA, 125, e27409
Edberg, N. J., Brain, D. A., Lester, M., et al. 2009, AnGeo, 27, 3537
Edberg, N. J., Lester, M., Cowley, S. W., & Eriksson, A. I. 2008, JGRA, 113, A08206
Fang, X., Ma, Y., Lee, Y., et al. 2020, JGRA, 125, e26838
Fang, X., Ma, Y., Masunaga, K., et al. 2017, JGRA, 122, 4117
Fedorova, A., Bertaux, J. L., Betsis, D., et al. 2018, Icar, 300, 440
Fedorova, A., Montmessin, F., Korablev, O., et al. 2021, JGRE, 126, e06616
Felici, M., Withers, P., Smith, M. D., et al. 2020, JGRA, 125, e27083
Frahm, R. A., Sharber, J. R., Winningham, J. D., et al. 2006a, SSRv, 126, 389
Frahm, R. A., Sharber, J. R., Winningham, J. D., et al. 2010, Icar, 206, 50
Frahm, R. A., Winningham, J. D., Sharber, J. R., et al. 2006b, Icar, 182, 371
Gao, J., Rong, Z., Klinger, L., et al. 2021, E&SS, 8, e01860
Garnier, P., Jacquey, C., Gendre, X., et al. 2022a, JGRA, 127, e30147
Garnier, P., Jacquey, C., Gendre, X., et al. 2022b, JGRA, 127, e30146
Gruesbeck, J. R., Espley, J. R., Connerney, J. E., et al. 2018, JGRA, 123, 4542
Halekas, J. S., Brain, D. A., Luhmann, J. G., et al. 2017, JGRA, 122, 6240
Hall, B. E., Lester, M., Sánchez-Cano, B., et al. 2016, JGRA, 121, 11474
Hall, B. E., Sánchez-Cano, B., Wild, J. A., Lester, M., & Holmström, M. 2019, JGRA, 124, 4761
Jordan, R., Picardi, G., Plaut, J., et al. 2009, P&SS, 57, 1975
Kimura, T., Tsuchiya, F., Murakami, G., & Yamazaki, A. 2022, NatCo, 13, 6609
Kleinböhl, A., Kass, D. M., Schofield, J. T., & McCleese, D. J. 2014, in Eighth Int. Conf. on Mars (Pasadena, CA: Lunar and Planetary Institute), 1144
McCleese, D. J., Schofield, J. T., Taylor, F. W., et al. 2007, JGRE, 112, E05S06
Mitchell, D. L., Lin, R. P., Mazelle, C., et al. 2001, JGR, 106, 23419
Nagy, A. F., Winterhalter, D., Sauer, K., et al. 2004, SSRv, 111, 33
Neves-Amaral, L., Kajdic, P., Sanchez-Cano, B., Bernal, C. G., & Rojas-Castillo, D. 2019, MmSAI, 90, 639
Odstrcil, D. 2003, AdSpR, 32, 497
Orosei, R., Jordan, R. L., Morgan, D. D., et al. 2015, P&SS, 112, 98
Qin, J. F., Zou, H., Ye, Y. G., et al. 2019, JGRE, 124, 602
Romanelli, N., Bertucci, C., Gõmez, D., & Mazelle, C. 2015, JGRA, 120, 7737
Sanchez-Cano, B., Morgan, D. D., Witasse, O., et al. 2015, JGRA, 120, 2166
Sánchez-Cano, B., Narvaez, C., Lester, M., et al. 2020, JGRA, 125, e28145
Sánchez-Cano, B., Radicella, S. M., Herraiz, M., Witasse, O., & Rodríguez-Caderot, G. 2013, Icar, 225, 236
Shinagawa, H., & Cravens, T. E. 1989, JGR, 94, 6506
Shirley, J. 2015, Icar, 251, 128
Tao, C., Budnik, E., Bouchemit, M., et al. 2015, In Situ Parameters Propagated from the Earth to Mars [dataset]. Ovgso, doi:10.6096/2001
Tao, C., Ryuho, K., Fukunishi, H., Takahashi, Y., & Yokoyama, T. 2005, JGRA, 110, A11208
Trotignon, J. G., Mazelle, C., Bertucci, C., & Acuña, M. H. 2006, P&SS, 54, 357
USGS 2023, Mars MGS MOLA DEM 463m, https://astrogeology.usgs.gov/search/map/mars_mgs_mola_dem_463m
Venkateswara Rao, N., Leelavathi, V., Mohanamanasa, P., Haider, S. A., & Rao, S. V. 2019, JGRA, 124, 3007
Vignes, D., Mazelle, C., Rme, H., et al. 2000, GeoRL, 27, 49
Wang, H., & Richardson, M. I. 2015, Icar, 251, 112
Wang, M., Lee, L. C., Xie, L., et al. 2021, A&A, 651, A22
Wang, M., Xie, L., Lee, L. C., et al. 2020, ApJ, 903, 125
Withers, P. 2009, AdSpR, 44, 277
Xu, S., Liemohn, M., Bougher, S., & Mitchell, D. 2015, GeoRL, 42, 9702
Xu, S., Mitchell, D. L., McFadden, J. P., et al. 2023, JGRA, 128, e2023JA031353
Zhang, T. L., Schwingenschuh, K., Russel, C. T., & Luhmann, J. G. 1991, GeoRL, 18, 127
Zurek, R. W., & Smrekar, S. E. 2007, JGRE, 112, E05S01